



11 ABSTRACT: We investigate the properties of relative dispersion of Lagrangian particles in a  
12 global-ocean simulation resolving both inertia-gravity waves (IGW) and meso and submesoscale  
13 (M/SM) turbulence. More specifically, we test if the dispersion laws depend on the shape of the  
14 Eulerian kinetic energy spectrum, as predicted from quasi-geostrophic turbulence theory. To this  
15 end, we focus on two areas, in the Kuroshio Extension and in the Gulf Stream, for which the  
16 relative importance of IGW compared to M/SM vary in summer and winter. In winter, Lagrangian  
17 statistical indicators return a picture in overall agreement with the shape of the kinetic energy  
18 spectrum. Conversely, in summer, when submesoscales are less energetic and higher-frequency  
19 internal waves gain importance, the expected relations between dispersion properties and spectra  
20 do not seem to hold. This apparent discrepancy is explained by decomposing the flow into nearly-  
21 balanced motions and internal gravity waves, and showing that the latter dominate the kinetic energy  
22 spectrum at small scales. Our results are consistent with the hypothesis that high-frequency IGWs  
23 do not impact relative dispersion, which is then controlled by the nearly-balanced, mainly rotational,  
24 flow component at larger scales. These results highlight that geostrophic velocities derived from  
25 wide-swath altimeters, such as SWOT, may present limits when estimating surface dispersion, and  
26 that current measuring satellite missions may provide the complementary information to do so.

## 27 **1. Introduction**

28 Ocean flows at lengthscales smaller than few hundreds of kilometers are composed of a rich  
29 variety of dynamical structures, e.g. fronts, eddies and internal gravity waves (IGW). On one  
30 hand, fronts and eddies constitute the so-called meso and submesoscales (M/SM), which evolve  
31 over timescales of days to weeks. On the other, IGWs are associated with more rapid (of the  
32 order of hours) temporal dynamics, which tend to interact with, and dampen, lower-frequency  
33 balanced motions (Barkan et al. 2017). Understanding these interactions is important, for instance  
34 for the interpretation and exploitation of new, high-resolution satellite-altimetry data (Uchida et al.  
35 2024) or the characterization of material transport at fine scales (Holmes-Cerfon et al. 2013;  
36 Hernández-Dueñas et al. 2021).

37 Although high-frequency motions, such as internal tides and gravity waves, are often considered  
38 to weakly contribute to the transport of tracers (see, e.g., Beron-Vera and LaCasce 2016), their effect  
39 on the dispersion of Lagrangian drifters remains poorly explored (Lumpkin et al. 2017), and the  
40 results do not seem completely conclusive. Relying on high-resolution numerical simulations in the  
41 south Atlantic ocean, it was argued that high-frequency motions considerably increase Lagrangian  
42 diffusivity, particularly at small scales (Sinha et al. 2019). However, Wang et al. (2018), using  
43 a non-hydrostatic numerical model representing both an upper mixed layer and internal waves,  
44 showed that while high-frequency motions may have an effect on pair dispersion rates, the details  
45 of this effect depend on the specific features of the M/SM dynamics.

46 Beyond their interest for material transport, Lagrangian studies also reveal useful to characterize  
47 the submesoscales, as shown in many regions of the world ocean. The link between Lagrangian  
48 measurements and statistical properties, as those quantified by the kinetic energy spectrum of the  
49 underlying flow, is then established through different bridging relations, obtained dimensionally  
50 in the framework of classical fluid-turbulence theory. The utility of this approach for quasi-  
51 geostrophic (QG) meso and submesoscale dynamics is well documented (LaCasce 2008; Berti  
52 et al. 2011; Poje et al. 2014; Corrado et al. 2017; Foussard et al. 2017). Assessing whether high-  
53 frequency motions affect particle dispersion regimes, and their possible impact on the validity of  
54 these bridging relations, thus remains a question of prime scientific interest.

55 If a possible limitation of Lagrangian data is their moderately sparse coverage, a global view of  
56 ocean-surface currents can be achieved through satellite-altimetry measurements. Conventional

57 instruments, however, were limited in spatial resolution to  $O(100)$  km (Morrow et al. 2023), which  
58 has not permitted, so far, the observation of structures in the submesoscale range, or even in the  
59 lower end of the mesoscale one. New-generation, wide-swath altimetry is pushing this limit to much  
60 smaller scales. Indeed, the Surface Water and Ocean Topography (SWOT) mission has recently  
61 started to provide sea surface height (SSH) data at an unprecedented resolution of (5 – 10) km (Fu  
62 et al. 2024). While this represents a major advancement in our ability to access the fine-scale range,  
63 the proper exploitation of these data also raises several important challenges. For instance, oceanic  
64 currents are retrieved from SSH assuming geostrophic balance. However the latter is not granted  
65 to hold at the smallest resolved scales, where ageostrophic and high-frequency motions may be  
66 expected to have a non-negligible dynamical signature (Yu et al. 2021). Determining with what  
67 accuracy (in terms of spatial scales) the velocity fields computed from SSH represent real surface  
68 currents, and their turbulent properties, then seems crucial. An interesting approach to address this  
69 point is to examine Lagrangian statistics, which reflect the temporal evolution of fluid parcels in  
70 the flow and hence sample processes acting on different timescales. This can be done, for instance,  
71 by comparing Lagrangian statistics from synthetic drifters advected by SWOT-derived velocities  
72 and real drifters (Tranchant et al. 2025). Another avenue of efforts, which is the one undertaken  
73 here, is to resort to high-resolution numerical simulations and to compare Lagrangian dispersion  
74 properties with their predictions from QG turbulence theory. In this case, the availability of the  
75 velocity field at high spatial and temporal resolution is expected to ease correlating Lagrangian  
76 diagnostics and Eulerian flow properties and, in the end, to disentangle contributions from the  
77 different physical processes at play.

78 In this work, we use high-resolution velocity fields from the MITgcm LLC4320 simulation (Forget  
79 et al. 2015), resolving submesoscales and accounting for IGWs, to advect Lagrangian tracer  
80 particles. We then characterize relative-dispersion statistics using different types of indicators,  
81 namely computed either at fixed time or at fixed lengthscale. More specifically, we aim to  
82 assess whether and how high-frequency motions impact the behavior of Lagrangian diagnostics,  
83 particularly testing the relation of the latter with the spectral kinetic energy of the Eulerian flow.  
84 We focus on the Kuroshio Extension region and examine the seasonal dependence of the results.  
85 As winter and summer lead to distinct features in terms of meso and submesoscale energetics, this  
86 will allow us to explore the sensitivity of the difference in intensity of M/SM motions compared to

87 IGWs. In order to test the generality of our main results, we then perform the same analysis also  
88 in another energetic region, close to the Gulf Stream.

89 This study extends previous ones (Maalouly et al. 2023, 2024), conducted in the framework of the  
90 idealized SQG<sup>+1</sup> model, a quasi-geostrophic model including next-order corrections in the Rossby  
91 number (Lapeyre 2017; Hakim et al. 2002). Those studies showed that including the ageostrophic  
92 flow component into particle advection has quite marginal effects on relative dispersion over long  
93 times (Maalouly et al. 2023, 2024). However, by construction, the SQG<sup>+1</sup> model only accounts for  
94 weak deviations from geostrophic balance and, therefore, does not include internal waves, which  
95 motivates the present investigation.

96 This article is organized as follows. Section 2 describes LLC4320 simulation and the setup of  
97 the Lagrangian-advection numerical experiments. Section 3 provides a characterization of the flow  
98 properties from Eulerian diagnostics in Kuroshio Extension. In Sec. 4 we examine the related  
99 Lagrangian pair-dispersion statistics. We then interpret these results through a decomposition of  
100 fluid motions into their IGW and M/SM components, relying on the computation of frequency-  
101 wavenumber energy spectra, in Sec.5. A discussion on the comparison with the results in the Gulf  
102 Stream region is provided in Sec. 6 and conclusions are drawn in Sec. 7.

## 103 **2. Numerical simulations**

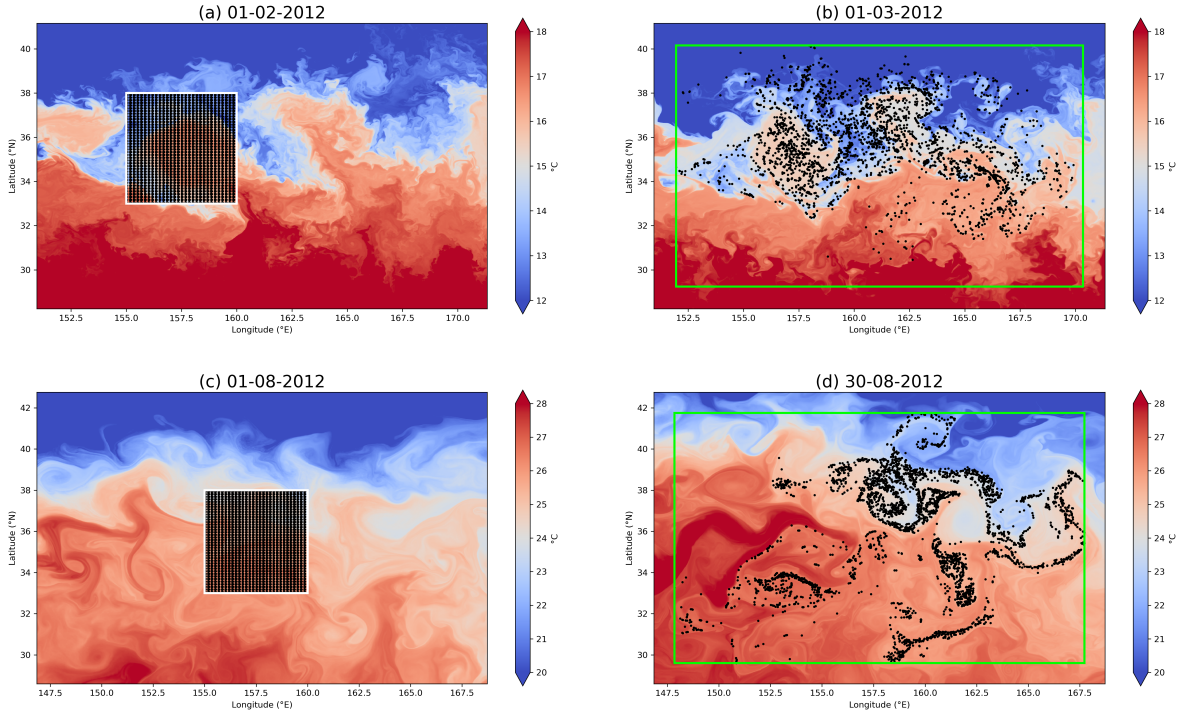
104 To explore the impact of high-frequency motions and submesoscales on Lagrangian dispersion,  
105 we use data from the global-ocean LLC4320 simulation (Forget et al. 2015) to simulate trajectories  
106 of synthetic particles. LLC4320 was performed using MITgcm (Marshall et al. 1997) with a  
107 horizontal spatial resolution of  $1/48^\circ$ , corresponding  $\approx 0.75$  km in polar regions to  $\approx 2.2$  km  
108 in equatorial ones. This resolution allows to resolve mesoscale dynamics and, to good extent,  
109 submesoscale ones. The model is tidally forced at different frequencies and was shown to reproduce  
110 diurnal and semidiurnal tidal variances with moderate biases compared to surface drifters (Yu et al.  
111 2019; Arbic et al. 2022; Caspar-Cohen et al. 2025). The output fields are available at hourly time  
112 intervals for a 1-year period spanning from September 13, 2011 to November 15, 2012. The model  
113 capabilities to realistically account for the above mentioned physical processes were extensively  
114 discussed in previous studies (see, e.g., Torres et al. 2018, 2022; Yu et al. 2019, 2021). Here we focus  
115 on the dynamics of Lagrangian tracer particles at the ocean surface. Particle advection is performed

116 offline by means of the Python OceanParcels package (Lange and van Sebille 2017; Zhang et al.  
117 2024), using the surface velocity fields extracted from LLC4320 simulation. The Lagrangian  
118 evolution equations are integrated using a fourth-order Runge-Kutta method and TRACMASS in  
119 space of the velocity field at particle positions (Döös et al. 2017; Delandmeter and Van Sebille  
120 2019).

121 In the following, we will examine two regions of the ocean (Kuroshio Extension and Gulf  
122 Stream). For each region, inside a square of side  $\approx 500$  km (as in Fig. 1a,c),  $N = 3600$  particles are  
123 initially uniformly distributed in triplets, each arranged in an equilateral triangle inscribed within  
124 a circle of radius 1 km. After their seeding, particles are tracked in time for a 30-day period during  
125 both February and August 2012, with hourly temporal resolution. For the statistical analysis of the  
126 relative dispersion process we consider only original pairs, meaning having a prescribed separation  
127 distance  $R_0$  at the seeding time.

### 128 **3. Eulerian flow properties of the Kuroshio Extension region**

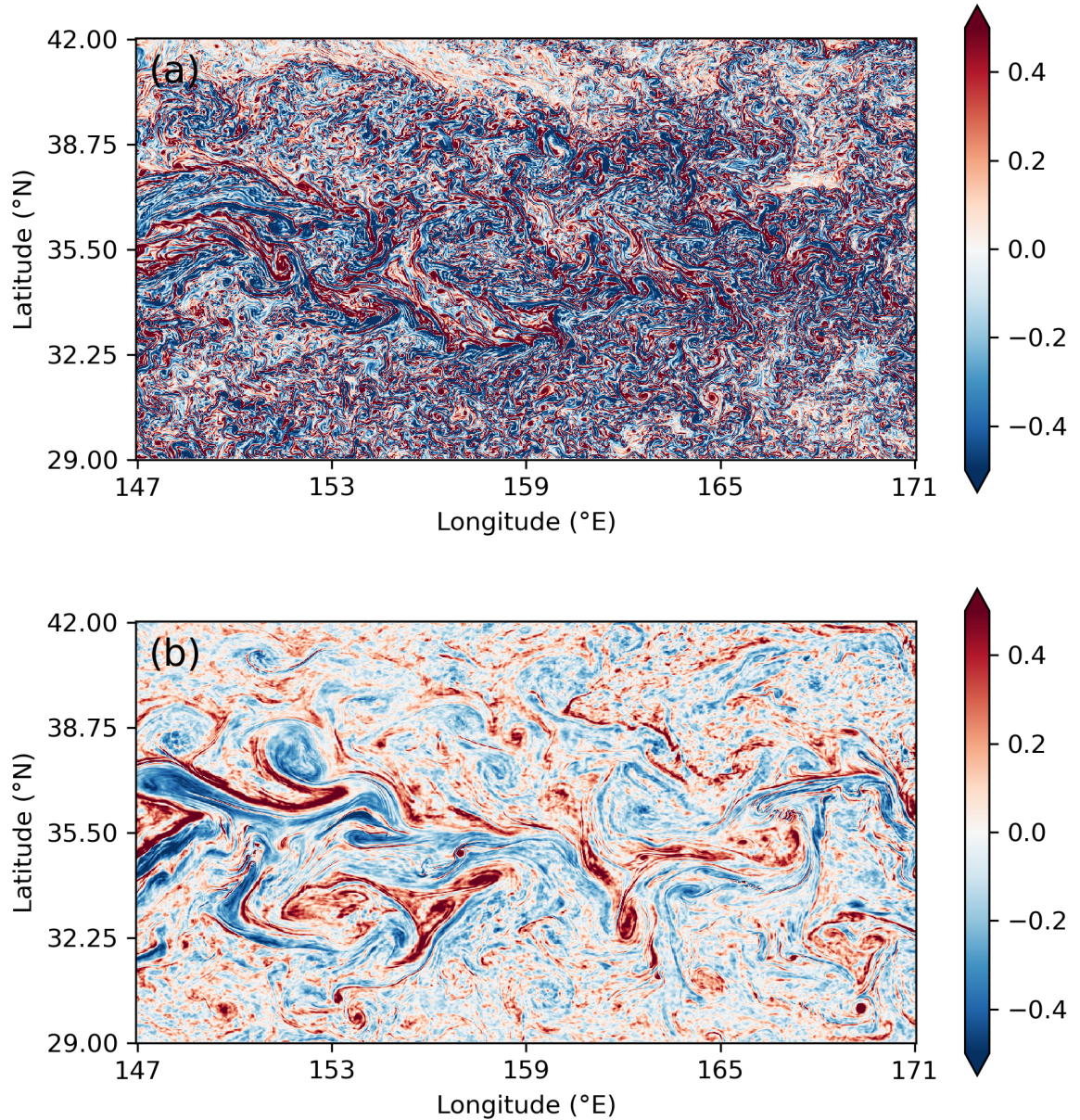
129 We start our analysis by presenting the region we are focusing on. Figure 1 shows sea surface  
130 temperature (SST) in both February (top row) and August (bottom row), at the beginning (left) and  
131 at the end (right) of the particle advection experiments. In both seasons, the region encompasses  
132 the Kuroshio current, as seen through its associated large-scale SST gradient with warm (cold)  
133 waters on the equatorward (poleward) side of the jet. In February, large meanders of the SST front  
134 indicate the presence of mesoscale structures, with a typical size of 150 to 400 km (Fig. 1a,b). In  
135 addition, a wealth a smaller eddies of  $O(10)$  km size, due to submesoscale instabilities, can also  
136 be seen along the large-scale SST front. On the contrary, in August (Fig. 1c,d) the latter fine scales  
137 seem to fade out. These observations are confirmed by inspection of relative-vorticity snapshots,  
138 shown in Fig. 2 at mid February and August (i.e. half the total Lagrangian integration time). While  
139 in winter a dense population of submesoscale eddies and filaments is clearly visible, to the point  
140 that larger scales are hardly detectable, in summer vorticity is mainly concentrated at mesoscales  
141 and has a smoother, much more filamentary structure. Note, too, the weaker SST gradients in  
142 August compared to February as well as smaller values of relative vorticity. Such seasonality is  
143 consistent with past numerical (Sasaki et al. 2014) and observational studies (Callies et al. 2015).



144 FIG. 1. Snapshots of the SST field in the Kuroshio Extension region in February (top line) and in August  
 145 (bottom line) at the beginning (a, c) and at the end (b, d) of the 30-day long Lagrangian experiments. The  
 146 corresponding particle distributions are shown with black dots. The green rectangles in (b, d) indicate the largest  
 147 area covered by particles on the latest day of the month.

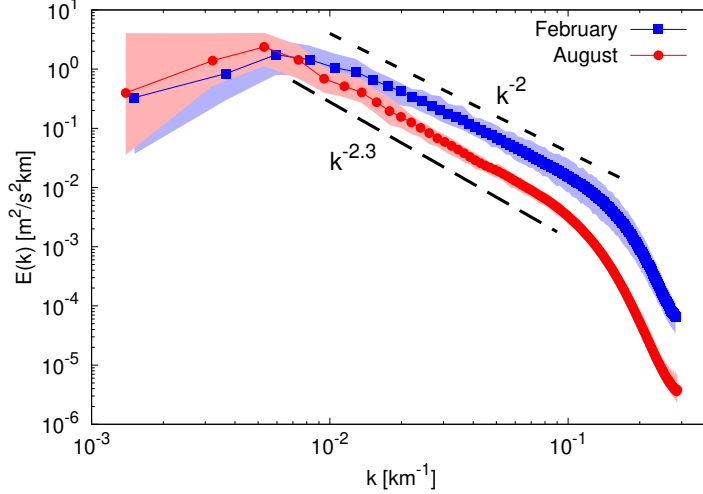
150 Since we aim at understanding how the behaviors of Lagrangian-dispersion indicators depend  
 151 on the Eulerian flow properties, it is important to properly select the spatial domain over which the  
 152 latter are computed. Considering that particles spread in time and distribute over a wider region  
 153 than the one in which they were released (see Fig. 1), for each month we decided to choose an area  
 154 including all the 3600 particles at the end of the Lagrangian-tracking experiment (green rectangles  
 155 in Fig. 1b and Fig. 1d). This ensures that Eulerian statistics reflect the properties of the velocity  
 156 field sampled by Lagrangian tracers.

157 The wavenumber spectra of horizontal kinetic energy, averaged in time over February and August  
 158 are presented in Fig. 3. They confirm that the flow in February is more energetic than in August,  
 159 particularly at scales smaller than 100 km. The winter kinetic energy spectrum scales approximately  
 160 as  $E(k) \sim k^{-2}$ , as often observed in the presence of energetic submesoscales (Klein et al. 2008;  
 161 Capet et al. 2008), over slightly more than a decade of wavenumbers. Note, however, that due to the



148 FIG. 2. Snapshots of relative vorticity, normalized by the Coriolis parameter,  $\zeta/f$  in the Kuroshio Extension  
 149 region, for February 15, 2012 (a) and August 15, 2012 (b).

162 non-negligible uncertainties on  $E(k)$ , particularly at small scales, the spectral slope  $\beta$  from a fit [for  
 163  $k$  between  $O(10)$  km and  $O(100)$  km] varies in the range  $5/3 \lesssim \beta \lesssim 2.4$ , depending on the specific  
 164 extension of the fitting range. The summer spectrum is characterized by smaller uncertainties



167 FIG. 3. Wavenumber spectra of horizontal kinetic energy, averaged over February (blue squares) and August  
 168 (red dots), in the Kuroshio Extension region. For each month, the shaded areas represent the temporal variability  
 169 of the spectrum. The reference lines  $k^{-2}$  and  $k^{-2.3}$  are also shown for comparison.

165 (except at the largest scales), and its scaling behavior is close to  $k^{-2.3}$  over a wavenumber range of  
 166 comparable width.

#### 170 4. Lagrangian pair-dispersion statistics in Kuroshio Extension

171 After having described the main features of the Eulerian flow, we present in this section the  
 172 results about Lagrangian pair-dispersion statistics. We recall that we consider only original pairs,  
 173 with an initial separation distance  $R_0 \approx 3.48$  km. Distances between particles at different times are  
 174 computed on the sphere using Haversine formula. Uncertainties on the considered indicators are  
 175 estimated as the 95% confidence interval of the bootstrapped mean of 1000 samples.

176 A natural approach to analyze pair-separation processes is to measure the mean-square relative  
 177 displacement between two particles as a function of time, i.e. relative dispersion

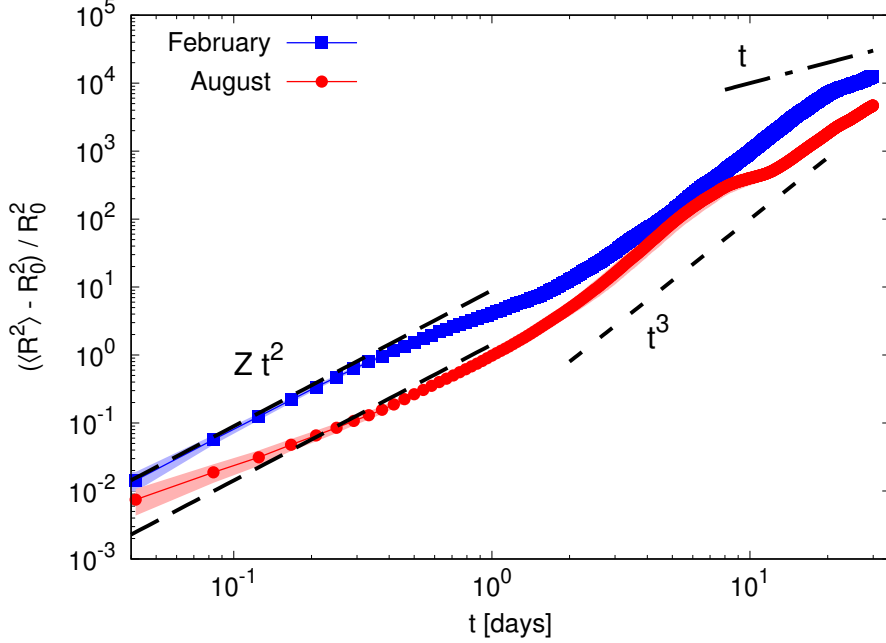
$$\langle R^2(t) \rangle = \langle |\mathbf{x}_i(t) - \mathbf{x}_j(t)|^2 \rangle. \quad (1)$$

178 In the above expression,  $i = 1, \dots, N$  labels a given particle among the  $N$  considered ones, whose  
 179 position evolves according to  $\dot{\mathbf{x}}_i = \mathbf{u}(\mathbf{x}_i(t), t)$ , with  $\mathbf{u} = (u, v)$  the horizontal surface velocity. The an-

180 gular brackets indicate an average over all  $i$  and all corresponding particles  $j$  with initial separation  
 181  $|\mathbf{x}_i(0) - \mathbf{x}_j(0)| = R_0$ , so that  $\langle R^2(0) \rangle = R_0^2$ .

182 We first recall the expected behavior of  $\langle R^2(t) \rangle$  obtained from dimensional arguments, for homo-  
 183 geneous isotropic incompressible two-dimensional turbulence . As extensively documented (see,  
 184 e.g., Babiano et al. 1990; Foussard et al. 2017) these expectations may be difficult to observe  
 185 for different reasons, such as a finite inertial range of the energy and enstrophy cascades, or the  
 186 sensitivity of  $\langle R^2(t) \rangle$  to the distance of the initial pair separation. At short enough times, relative  
 187 dispersion is expected to grow in a ballistic way,  $\langle R^2(t) \rangle \simeq R_0^2 + Z R_0^2 t^2$  (Batchelor 1950; Babiano  
 188 et al. 1990). Here  $Z = \langle \zeta^2/2 \rangle_x$  is relative enstrophy,  $\langle \dots \rangle_x$  denotes a spatial average, and vorticity is  
 189 related to the horizontal flow by  $\zeta = \partial_x v - \partial_y u$ . Later in time, when the pair separation distance is  
 190 intermediate between the smallest and the largest eddy sizes, the temporal growth of  $\langle R^2(t) \rangle$  can  
 191 be dimensionally linked to the shape of the kinetic energy spectrum  $E(k)$ . Assuming a power-law  
 192 scaling  $E(k) \sim k^{-\beta}$ , if the spectrum is sufficiently steep ( $\beta > 3$ ) relative dispersion should grow  
 193 exponentially in time, with a rate proportional to  $Z^{1/2}$ . Such fast decay of kinetic energy with  
 194 wavenumber, typical of weakly-energetic submesoscales, implies that strain is localized at large  
 195 scale and, hence, that the pair-separation process is controlled by the largest flow features (Fous-  
 196 sard et al. 2017). If instead  $1 < \beta < 3$ , i.e. for energetic submesoscales, a power-law behavior  
 197  $\langle R^2(t) \rangle \sim t^{4/(3-\beta)}$  is expected. This is often called a local dispersion regime, because the growth of  
 198  $\langle R^2(t) \rangle$  is in this case driven by velocity differences over lengthscales comparable with the distance  
 199 between the two particles in a pair (see, e.g., LaCasce 2008). Clearly, this situation includes the  
 200 well-known Richardson dispersion regime,  $\langle R^2(t) \rangle \sim t^3$ , corresponding to  $E(k) \sim k^{-5/3}$ . At even  
 201 larger times, when the pair-separation distance overcomes the largest eddy size, particles experience  
 202 uncorrelated velocities and thus relative dispersion follows a slower, standard-diffusion behavior,  
 203  $\langle R^2(t) \rangle \sim t$ .

204 For the Kuroshio Extension region, relative dispersion as a function of time is shown in Fig. 4,  
 205 after subtracting the initial value  $R_0$  and normalizing by it. At short times, we observe a behavior  
 206 close to the expected ballistic regime,  $(\langle R^2 \rangle - R_0^2) / R_0^2 \approx Z t^2$ , with  $Z$  independently computed from  
 207 the Eulerian velocity field. The agreement with the theoretical prediction is better in February  
 208 than in August (for which a slower initial growth is observed) but the prediction gives the right  
 209 magnitude for both seasons. We do not have an interpretation of this deviation from the ballistic



220 FIG. 4. Normalized relative dispersion  $(\langle R^2 \rangle - R_0^2)/R_0^2$  as a function of time, for February and August in  
 221 the Kuroshio Extension region. Uncertainties, estimated as the 95% confidence interval from a bootstrapping  
 222 procedure, are represented by the shading.

210 behavior but remark that it only concerns a time range when the uncertainty on relative dispersion  
 211 is also larger. The larger values of relative dispersion at short times, and hence of enstrophy, in  
 212 winter than in summer align with the observation of generally more energetic small-scale flows in  
 213 this season (see Fig. 2).

214 At intermediate times ( $1 \text{ days} < t < 10 \text{ days}$ ), in February,  $\langle R^2(t) \rangle$  follows a behavior not far from  
 215 the Richardson  $t^3$  law, before a transition to a linear, diffusive scaling at larger times. In August,  
 216 within the same intermediate time range, relative dispersion increases more rapidly (with a slightly  
 217 steeper slope) before eventually transitioning to what appears to be a  $t^3$  scaling. If in terms of  
 218 dispersion regimes the resulting picture qualitatively agrees with the spectra shown in Fig. 3, from  
 219 a quantitative point of view the situation is less clear.

223 A connected metric of dispersion is relative diffusivity,

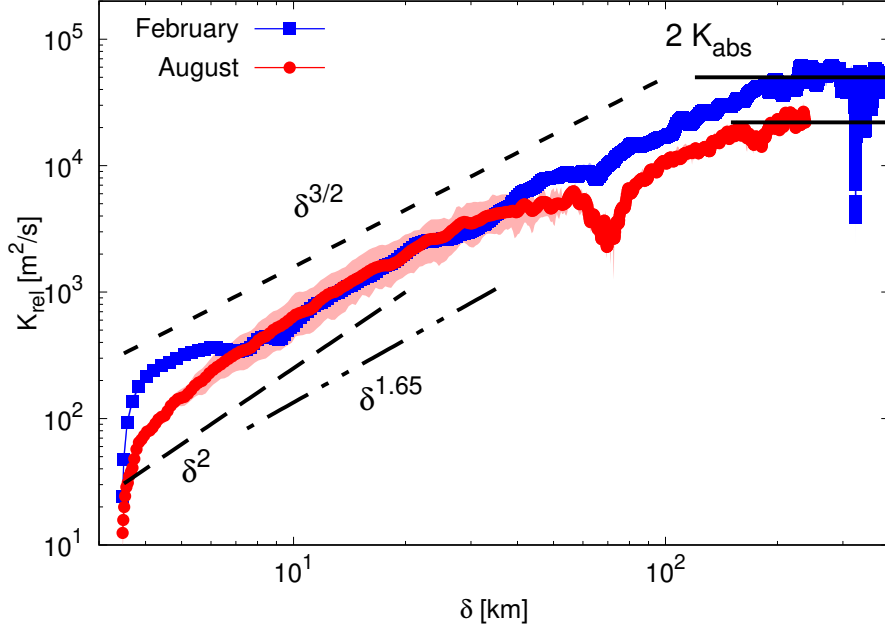
$$K_{rel} = \frac{1}{2} \frac{d\langle R^2(t) \rangle}{dt}. \quad (2)$$

224 While clearly by definition  $K_{rel}$  is still a function of time, it is often useful to plot it as a function  
225 of the distance  $\delta = \langle R^2(t) \rangle^{1/2}$ . The results are shown in Fig. 5. We preliminarily remark that at the  
226 largest separations [ $\delta > O(100)$  km], relative diffusivity approaches a constant value, as expected.  
227 In this range, one finds that indeed  $K_{rel} \approx 2K_{abs}$ , where  $K_{abs}$  is absolute diffusivity (not shown).  
228 In February, at intermediate scales ( $10 \text{ km} < \delta < 100 \text{ km}$ ),  $K_{rel}$  quite closely follows a  $\delta^{3/2}$  scaling,  
229 indicative of a local dispersion regime, and corresponding to a kinetic energy spectrum  $E(k) \sim k^{-2}$ ,  
230 in agreement with the measured one (Fig. 3). In August, for scales between approximately 10 and  
231 40 km, relative diffusivity behaves similarly to the February scaling. In this range, taking into  
232 account uncertainties, it is not possible to distinguish between this behavior and the  $\delta^{1.65}$  behavior  
233 corresponding to the spectral slope  $\beta = 2.3$ . Then  $K_{rel}$  decreases for increasing  $\delta$ , in agreement with  
234 Fig. 4 where a slow-down of relative dispersion can be seen at around 10 days. This seems to be  
235 associated with a change in the regime of growth of  $\langle R^2(t) \rangle$ , which might be due to efficient particle  
236 retention in mesoscale eddies. More importantly, when approaching submesoscales (particularly  
237 for  $\delta < 20$  km), we observe a tendency towards a steeper growth, compatible with  $K_{rel} \sim \delta^2$ . The  
238 latter behavior points to nonlocal dispersion and, dimensionally, it corresponds to a smooth flow  
239 with  $\beta > 3$ . Therefore, it is at odds with the spectral slope  $\beta = 2.3$  measured in summer (Fig. 3), a  
240 fact that deserves further investigation by means of other indicators.

246 Another indicator, equally based on a straightforward fixed-time analysis, useful to discriminate  
247 between different dispersion regimes, is the kurtosis of the probability density function (pdf) of  
248 the pair separation distance (LaCasce 2008, 2010; Foussard et al. 2017),

$$ku(t) = \frac{\langle R^4(t) \rangle}{\langle R^2(t) \rangle^2}. \quad (3)$$

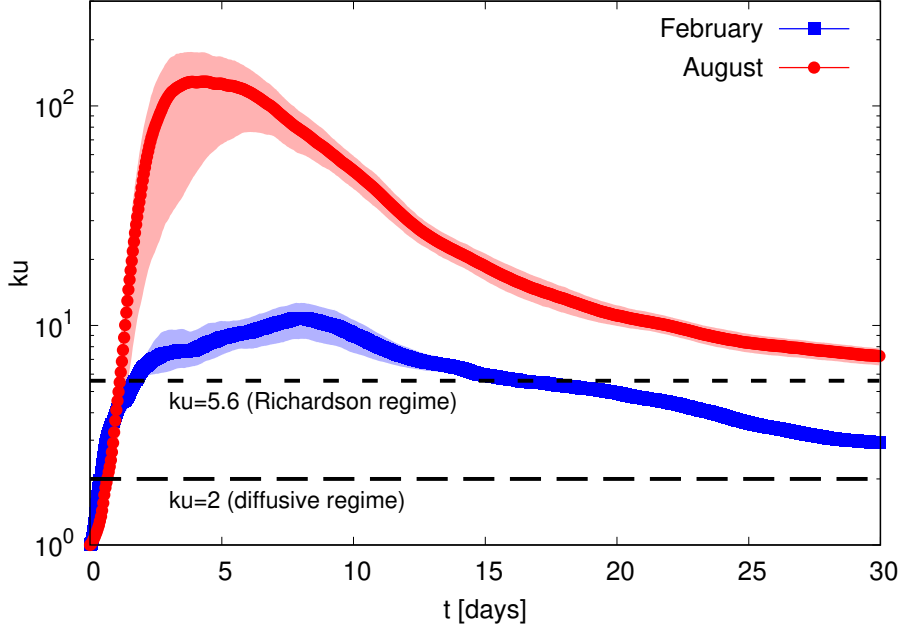
249 In a nonlocal dispersion regime, the kurtosis is expected to display fast, exponential growth. For  
250 local dispersion, it should level off around a constant value over a finite interval of time [e.g.,  
251  $ku(t) = 5.6$  for Richardson dispersion]. At larger times, in the diffusive regime, one expects  
252  $ku(t) = 2$ . As compared to relative dispersion and diffusivity, in the kurtosis temporal evolution  
253 the differences between winter and summer are much more evident (Fig. 6). At short times, the  
254 kurtosis grows to values an order of magnitude larger in August than in February, following a  
255 quasi-exponential regime. In February, after a rapid increase, kurtosis attains an almost constant  
256 plateau at around 15 days, with a value close to  $ku = 5.6$ , the Richardson expectation, before



241 FIG. 5. Relative diffusivity  $K_{rel}$  as a function of the separation distance  $\delta = \langle R^2(t) \rangle^{1/2}$ , for February and  
 242 August in the Kuroshio Extension region. The  $\delta^{3/2}$  (short-dashed line),  $\delta^{1.65}$  (dashed-dotted line) and  $\delta^2$  (long-  
 243 dashed line) behaviors correspond to  $\beta = 2$ ,  $\beta = 2.3$  and  $\beta > 3$ , respectively. The horizontal black solid lines  
 244 represent twice absolute diffusivity at large times,  $2K_{abs}$  (in each month). Uncertainties are estimated as the  
 245 95% confidence interval from a bootstrapping procedure.

257 decreasing. These observations then support those from relative diffusivity, suggesting that in  
 258 winter dispersion is local, while in summer it is nonlocal.

261 The computation of the previous diagnostics requires performing averages over pairs at any  
 262 given time along particle trajectories. It is known that such a procedure has some drawbacks,  
 263 due to the fact that dispersion regimes change in correspondence with lengthscales, not temporal  
 264 ones (Berti et al. 2011; Cencini and Vulpiani 2013). As a consequence, fixed-time statistics may  
 265 be biased by the superposition of different behaviors, due to distinct pairs experiencing different  
 266 dispersion regimes at the same, common time. Fixed-scale analyses, based on computing statistics  
 267 as a function of the length scales, instead, allow disentangling different dispersion regimes (see  
 268 Cencini and Vulpiani 2013, for a review). Therefore, we will now consider the finite-size Lyapunov  
 269 exponent (FSLE) (Aurell et al. 1997; Artale et al. 1997), namely a scale-by-scale dispersion rate



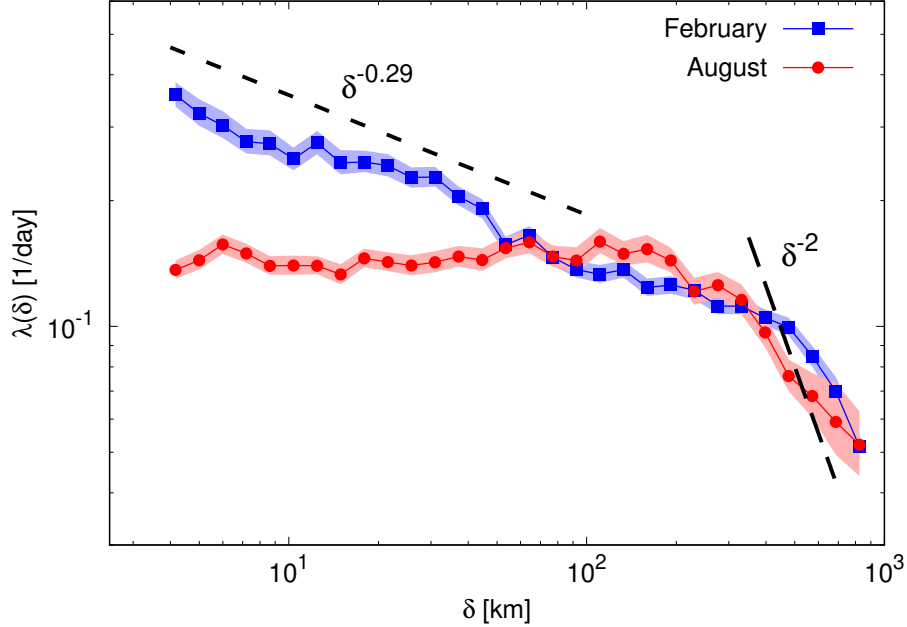
259 FIG. 6. Kurtosis of separation  $ku$  as a function of time, for February and August in the Kuroshio Extension  
 260 region. Uncertainties are estimated as the 95% confidence interval from a bootstrapping procedure.

270 defined as

$$\lambda(\delta) = \frac{\ln r}{\langle \tau(\delta) \rangle}, \quad (4)$$

271 where the average is over all particle pairs and  $\tau(\delta)$  is the time needed for the separation distance  
 272 to grow from  $\delta$  to a scale  $r\delta$  (with  $r > 1$ ). As for relative dispersion, dimensional arguments  
 273 allow to link the FSLE behavior and the kinetic energy spectrum of the underlying flow. In a  
 274 nonlocal dispersion regime, corresponding to a spectral exponent  $\beta > 3$  and exponential particle  
 275 separation, the FSLE should be independent of  $\delta$ . Its constant value provides an estimate of the  
 276 maximum Lagrangian Lyapunov exponent and should be proportional to  $Z^{1/2}$ . For more energetic  
 277 small-scale flows, when  $1 < \beta < 3$ , dispersion is local and the FSLE scales as  $\lambda(\delta) \sim \delta^{(\beta-3)/2}$ . In  
 278 particular, Richardson dispersion ( $\beta = 5/3$ ) translates into  $\lambda(\delta) \sim \delta^{-2/3}$ . Finally, in the diffusive  
 279 regime, holding for separations larger than the largest eddies, one expects  $\lambda(\delta) \sim \delta^{-2}$ .

280 In February, from the smallest sampled separations up to  $\delta \simeq 100$  km, the FSLE follows the  
 281 scaling  $\delta^{-\gamma}$ , with  $\gamma \simeq 0.29$  from a fit between  $\delta = 4$  and 100 km (Fig. 7), further supporting the  
 282 indication of local dispersion, associated with energetic submesoscales. From the value of the  
 283 exponent  $\gamma$  one has  $\beta \simeq 2.4$ , larger than the mean value ( $\beta = 2$ ) of the slope measured from the



291 FIG. 7. FSLE  $\lambda(\delta)$  for February and August in the Kuroshio Extension region. The  $\delta^{-0.29}$  scaling behavior  
 292 (short-dashed line), from a fit in the range  $4 \text{ km} \leq \delta \leq 100 \text{ km}$ , corresponds to the spectral slope  $\beta \approx 2.4$  and  
 293 the  $\delta^{-2}$  scaling law (long-dashed line) to the diffusive limit. Uncertainties are estimated as the 95% confidence  
 294 interval from a bootstrapping procedure.

284 spectrum, but compatible with its upper bound. In contrast, in August, in the same range of  
 285 scales ( $5 \text{ km} \lesssim \delta \lesssim 100 \text{ km}$ ),  $\lambda(\delta)$  is virtually independent of  $\delta$ . This confirms, once more, the  
 286 essentially nonlocal character of dispersion in this season, in spite of the spectrum [ $E(k) \sim k^{-2.3}$ ]  
 287 being shallower than  $k^{-3}$ . Finally, in both winter and summer, the FSLE eventually approaches  
 288 a diffusive regime, indicated by a  $\delta^{-2}$  behavior, for  $\delta \gtrsim 300 \text{ km}$ . The latter scale is in reasonable  
 289 agreement with the size of the largest eddies,  $\ell_M \sim 1/k_M \approx 200 \text{ km}$ , estimated from the wavenumber  
 290  $k_M$  where the kinetic energy spectra peak (Fig. 3).

295 Summarizing, the picture emerging from this analysis indicates that seasonality has an important  
 296 role on Lagrangian dispersion in this region. In particular, the overall coherence, in each season,  
 297 of the different metrics considered highlights that in winter (February) dispersion is local, while in  
 298 summer (August) it is nonlocal. In winter, the scaling behaviors of the Lagrangian diagnostics tend  
 299 to align with the usual predictions from turbulence theory based on the slope of the kinetic energy  
 300 power spectrum. Specifically, to reasonable extent, they match the dimensional expectations based

301 on a power-law decay of the kinetic energy spectrum with an exponent  $\beta \gtrsim 2$ , as the one measured  
302 from the Eulerian velocity field. Relative dispersion is the only exception, presenting a slightly  
303 different scaling perhaps more compatible with  $\beta = 5/3$ , which is however not too far from the  
304 value estimated from other indicators. In summer, the kinetic energy spectrum has a (clearer) slope  
305  $\beta \simeq 2.3$ , which would predict local dispersion, in contrast with the Lagrangian results.

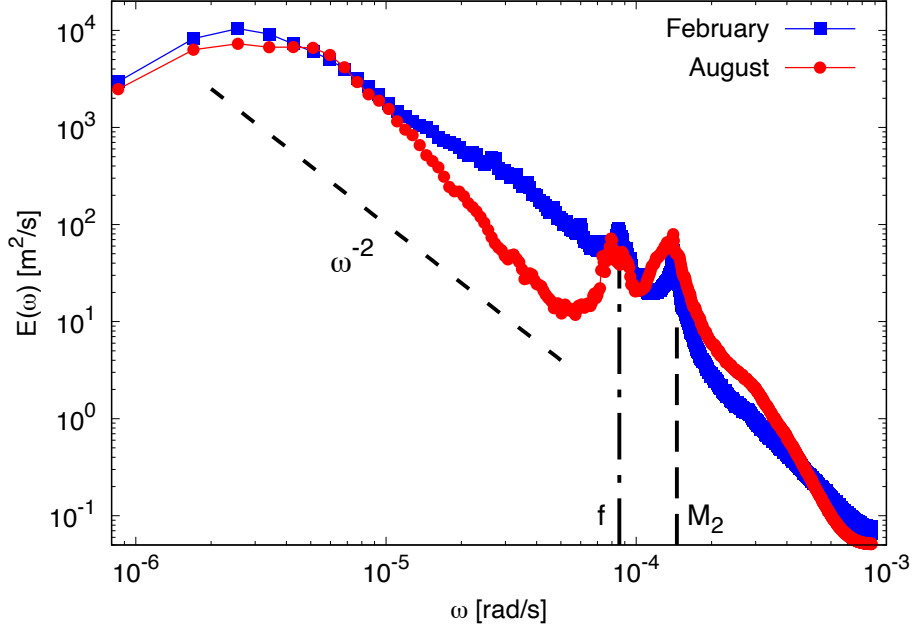
306 We conclude this section by noting that these findings appear in line with the visual inspection of  
307 Fig. 1, illustrating how particles disperse in the flow. After one month of simulation, Lagrangian  
308 particles tend to accumulate along fronts and inside large-scale vortices in summer (Fig. 1d) while  
309 they are more efficiently homogenized through the domain and at all scales in winter (Fig. 1b).  
310 Such a difference hints at Lagrangian transport driven by mesoscale fronts and eddies (i.e. nonlocal  
311 dispersion) in summer, and at smaller-scale fronts and eddies tending to disperse particles through  
312 the flow (as under local dispersion) in winter.

## 313 **5. Lagrangian dispersion interpretation based on a slow-fast flow decomposition**

314 The results in the previous section indicate that, in summer, there is a clear disagreement between  
315 relative dispersion indicators and their predictions from the kinetic energy spectrum, contrary to  
316 what one would expect within the theory of QG turbulence. Therefore, one question arises: what  
317 is the origin of such disagreement?

### 320 *a. Lagrangian frequency spectra*

321 One candidate to answer the above question is the presence of IGWs. A first way to determine  
322 their importance for the Lagrangian dynamics is to compute the Lagrangian frequency spectrum  
323 of kinetic energy  $E(\omega)$ . As observed in Fig. 8, for both February and August, the spectra peak  
324 at low frequencies, suggesting that the advection of Lagrangian particles is governed by slow  
325 (presumably quasi-balanced) motions. One can also clearly distinguish two peaks, corresponding  
326 to the Coriolis ( $f$ ) and tidal ( $M_2$ ) frequencies with periods  $T_f \approx 20.53$  h and  $T_{M_2} \approx 12.65$  h,  
327 respectively. In August, these peaks (most likely associated with IGWs) are more pronounced and  
328 constitute a significant part of the Lagrangian energy. This result highlights the fact that Lagrangian  
329 trajectories are sensitive to the high-frequency components of the flow. In February, on average,

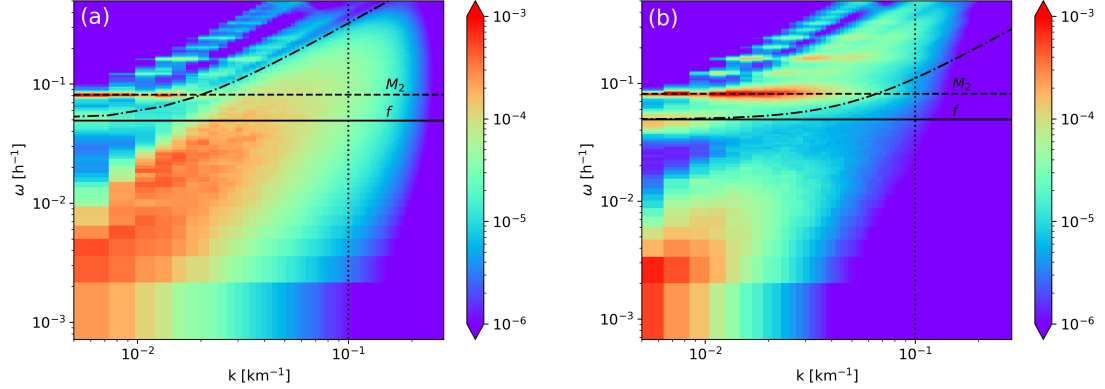


318 FIG. 8. Lagrangian frequency spectra of kinetic energy  $E(\omega)$  for February and August in the Kuroshio  
 319 Extension region. The vertical lines indicate the Coriolis ( $f$ ) and semidiurnal tidal ( $M_2$ ) frequencies.

320 the scaling of the spectrum is not far from  $\omega^{-2}$ , which corresponds to an exponential decay of the  
 321 velocity autocorrelation function (not shown).

### 322 *b. Frequency-wavenumber energy spectra*

323 We next analyze the respective contributions of M/SM motions and IGWs to the Eulerian kinetic  
 324 energy spectrum. Following the methodology of Torres et al. (2018, 2022), we compute the  
 325 frequency-wavenumber ( $\omega - k$ ) spectrum of kinetic energy, which is shown in Fig. 9a for February  
 326 and in Fig. 9b for August. The distinction between M/SM and IGWs can be made using the  
 327 dispersion-relation curve of IGWs,  $\omega^2 = c^2 k^2 + f^2$  (Torres et al. 2018). Here  $c$ ,  $k$ , and  $f$  are,  
 328 respectively, the phase speed of inertio-gravity waves, the isotropic horizontal wavenumber, and  
 329 the Coriolis frequency. This relation can be reformulated to incorporate the deformation radius  
 330  $L_R \approx c/|f|$ , leading to  $\omega^2 = f^2 (L_R^2 k^2 + 1)$  (Sutherland 2010). As seen in Fig. 9, using the dispersion  
 331 relation for the 10<sup>th</sup> vertical mode (dashed-dotted line) allows to make a clear distinction between  
 332 IGWs and balanced, M/SM motions. Indeed this mode corresponds to the highest baroclinic  
 333 mode resolved in the LLC4320 simulation and, hence, is the most relevant one for partitioning  
 334

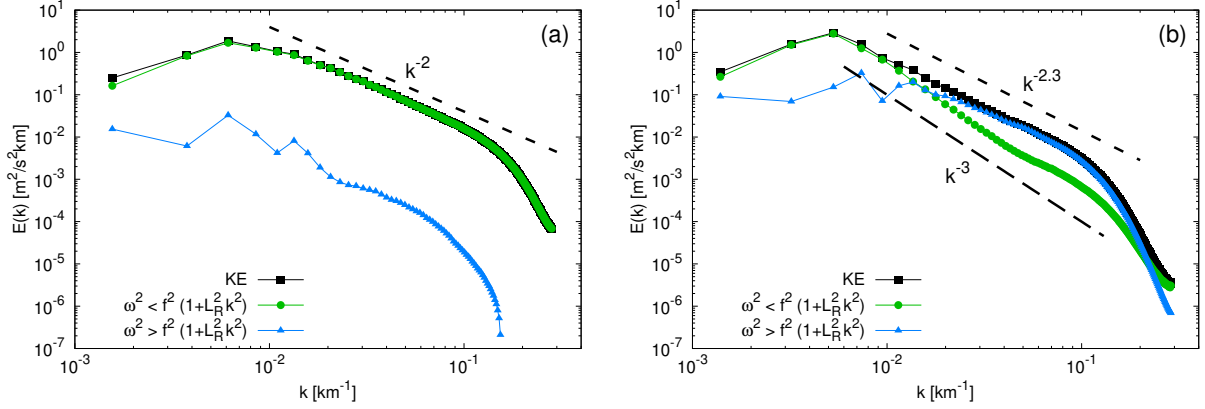


356 FIG. 9. Frequency-wavenumber spectra of kinetic energy  $E(k, \omega)$  in the Kuroshio Extension region during  
 357 February (a) and August (b); here spectra are shown in variance-preserving form  $k \omega E(k, \omega)$  with units in  
 358  $\text{m}^2 \text{s}^{-2}$ . The horizontal solid and dashed lines indicate the Coriolis ( $f$ ) and semidiurnal tidal ( $M_2$ ) frequencies,  
 359 respectively, while the dashed-dotted line shows the dispersion-relation curve for the 10<sup>th</sup> baroclinic mode. The  
 360 corresponding deformation radii are  $L_R = 65$  km (a) and  $L_R = 20$  km (b).

344 the flow into balanced and higher-frequency, wavy motions (Torres et al. 2018). In this region, its  
 345 value is  $L_R \simeq 65$  km in winter and  $L_R \simeq 20$  km in summer. This partitioning method is essential  
 346 because IGWs and high-frequency submesoscales share similar frequencies, making it difficult to  
 347 distinguish between them using simpler techniques, as e.g. filtering based solely on frequencies,  
 348 such as  $f$  or  $M_2$  (Jones et al. 2023).

349 In winter (Fig. 9a), the energy is concentrated at frequencies below those of IGWs, while internal  
 350 tides and inertial motions do not seem to contribute to it significantly. This suggests that the  
 351 energy is essentially all contained in M/SM motions. In summer (Fig. 9b), the energetic content  
 352 of high-frequency IGWs increases, with a marked concentration of energy around  $M_2$ , while that  
 353 of submesoscales considerably decreases. This is in line with the Lagrangian energy spectrum  
 354 (Fig. 8), for which we observe a spectral gap between the energetic low-frequencies and the inertial  
 355 and semidiurnal motions.

361 From the frequency-wavenumber spectrum  $E(k, \omega)$ , we can evaluate the IGW contributions to the  
 362 wavenumber spectrum of kinetic energy  $E(k)$  by integrating  $E(k, \omega)$  over frequencies satisfying  
 363 only either  $\omega^2 < f^2(1 + L_R^2 k^2)$  or  $\omega^2 > f^2(1 + L_R^2 k^2)$ . This procedure reveals that in February  
 364 (Fig. 10a) IGWs are less energetic than M/SM motions by two orders of magnitude. The latter,



375 FIG. 10. Decomposition of the kinetic energy wavenumber spectra  $E(k)$  for February (a) and August (b) in  
 376 the Kuroshio Extension region. The spectrum of the total kinetic energy (KE) is shown by black square points.  
 377 The contribution from frequencies such that  $\omega^2 < f^2(1 + L_R^2 k^2)$  corresponds to the green dots, while the blue  
 378 triangles are for frequencies  $\omega^2 > f^2(1 + L_R^2 k^2)$ . The corresponding deformation radii are  $L_R = 65$  km (a) and  
 379  $L_R = 20$  km (b). The reference lines  $k^{-2}$  in (a),  $k^{-3}$  and  $k^{-2.3}$  in (b), are also shown for comparison.

365 then, indeed account for most of the kinetic energy in the surface flow at all scales: the associated  
 366 spectrum is almost identical to that of the total kinetic energy, and both approximately follow a  
 367  $k^{-2}$  scaling. In August (Fig. 10b), instead, we observe that at small wavenumbers (lengthscales  
 368  $> 100$  km), mesoscale motions still dominate, but at larger wavenumbers (lengthscales  $< 50$  km),  
 369 submesoscales become less energetic and IGWs provide the leading contribution to the kinetic  
 370 energy spectrum. The small-scale IGW spectrum scales as  $k^{-2.3}$ , while that of low-frequency  
 371 (M/SM) motions behaves as  $k^{-3}$  up to  $k = 0.04$   $\text{km}^{-1}$ . Such steeper spectrum (from M/SM)  
 372 corresponds theoretically to a regime of nonlocal particle dispersion. This result is thus consistent  
 373 with IGWs having little to no effect on relative dispersion, despite having a prominent signature  
 374 on the small-scale energetic content of the flow.

### 380 c. Decomposition into rotational and divergent motions

381 To obtain a finer picture of what dynamical processes affect Eulerian spectra, kinetic energy  
 382 can be decomposed into rotational ( $\text{KE}_\zeta$ ) and divergent ( $\text{KE}_\Delta$ ) components, using Helmholtz

383 decomposition (Bühler et al. 2014; Rocha et al. 2016; Torres et al. 2018):

$$KE_{\zeta}(k) = \frac{1}{2} \int \frac{|\hat{\zeta}(k, \omega)|^2}{k^2} d\omega \quad (5)$$

384 and

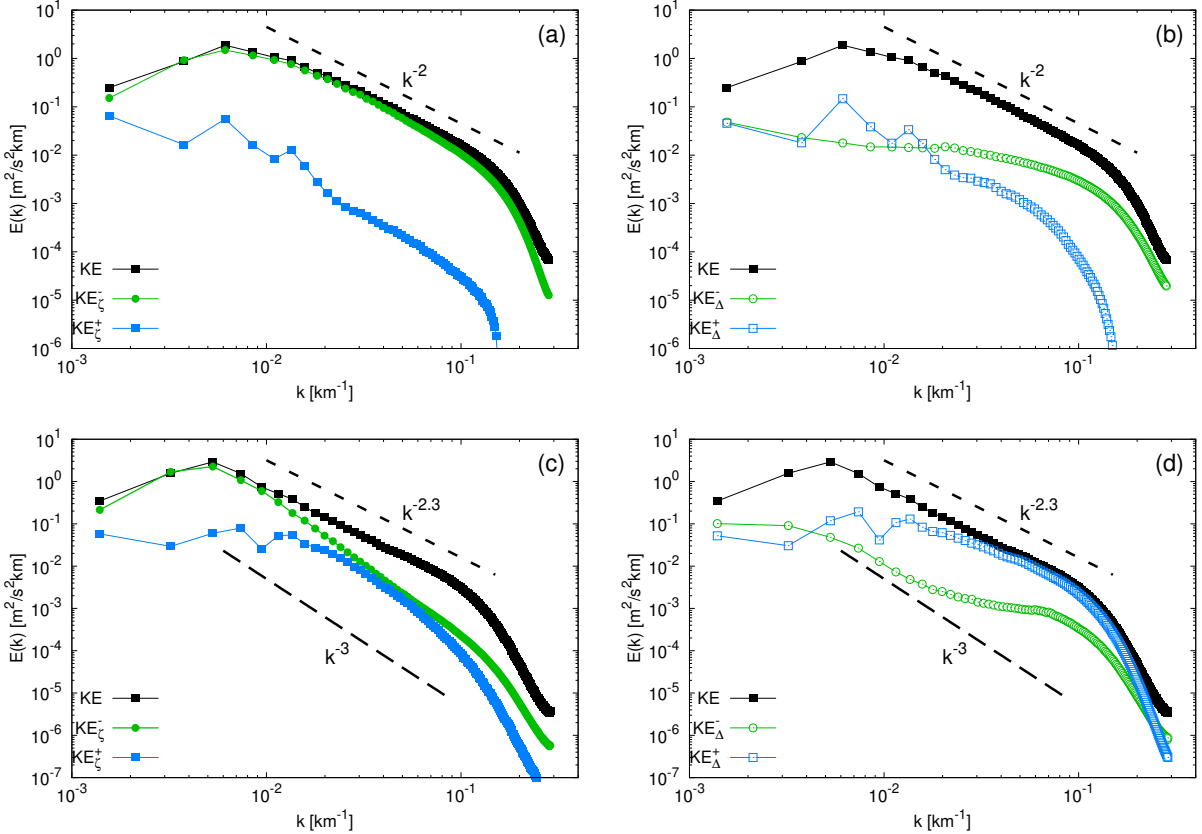
$$KE_{\Delta}(k) = \frac{1}{2} \int \frac{|\hat{\Delta}(k, \omega)|^2}{k^2} d\omega, \quad (6)$$

385 where  $\hat{\zeta}(k, \omega)$  and  $\hat{\Delta}(k, \omega)$  are the spatiotemporal Fourier transforms of vorticity  $\zeta$  and divergence  
 386  $\Delta = \partial_x u + \partial_y v$ , respectively. Mesoscale motions are typically close to geostrophic balance and hence  
 387 nondivergent. On the other hand, in general, both submesoscales (induced by frontal dynamics)  
 388 and IGWs contribute to the divergence field. We then further separate each component into  $KE_{\zeta, \Delta}^-$ ,  
 389 representing low-frequency processes such that  $\omega^2 < f^2(1 + L_R^2 k^2)$ , and  $KE_{\zeta, \Delta}^+$ , representing high-  
 390 frequency processes such that  $\omega^2 > f^2(1 + L_R^2 k^2)$ .

391 Figure 11 shows the results of this partitioning for February [panels (a) and (b)] and August  
 392 [panels (c) and (d)]. In February, the flow is dominated by its rotational component, primarily from  
 393 M/SM motions (Fig. 11a). At all scales, the divergent component from both M/SM and IGWs  
 394 contributes little to the overall kinetic energy (Fig. 11b). In August, the situation is different. At low  
 395 wavenumbers [lengthscales  $> (50 - 100)$  km], rotational M/SM motions dominate (Fig. 11c), while  
 396 at higher wavenumbers the divergent contribution from IGWs becomes dominant in the kinetic  
 397 energy spectrum (Fig. 11d). Notably, the spectrum of slow motions associated with vorticity  $KE_{\zeta}^-$   
 398 has, in this season, a clear  $k^{-3}$  scaling over an extended wavenumber range. The corresponding  
 399 spectrum of fast IGWs  $KE_{\zeta}^+$  is generally shallower, with values smaller than those of  $KE_{\zeta}^-$ , except  
 400 in a narrower range of scales where it is comparable (and behaves similarly) to  $KE_{\zeta}^-$ . These  
 401 results clearly show that the full wavenumber kinetic energy is not necessarily representative of the  
 402 balanced dynamics.

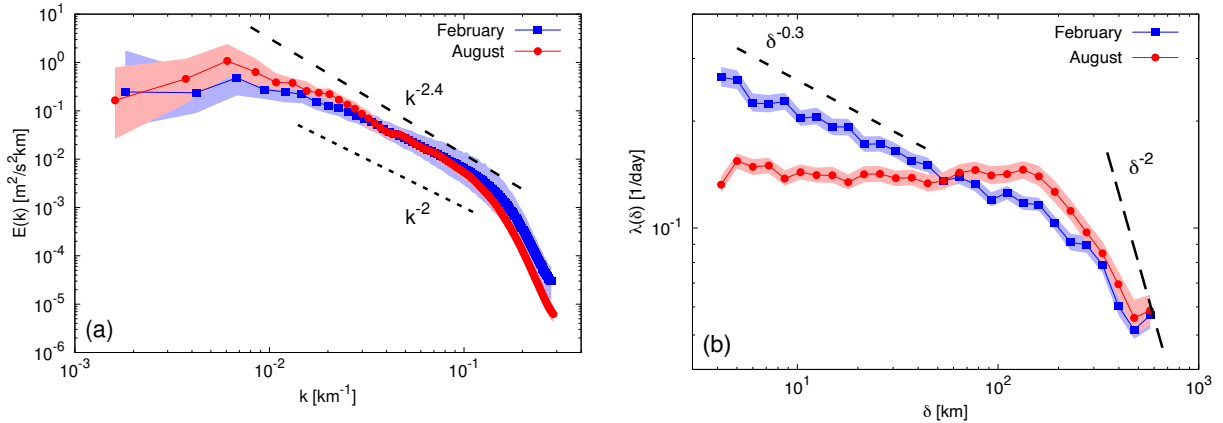
## 407 6. Comparison with results in the Gulf Stream region

408 In order to test the generality of the results in Sec. 4 and Sec. 5, here we provide a discussion of  
 409 the main picture emerging from the same approach in another energetic region, close to the Gulf  
 410 Stream. Its exact location and a more extensive characterization of the Eulerian and Lagrangian  
 411 properties for this case study are reported in Appendix A.



403 FIG. 11. Wavenumber spectra of kinetic energy  $E(k)$  in the Kuroshio Extension region. The spectrum of the  
 404 total kinetic energy (KE) is shown by black square points. (a, c) Spectra of the rotational component  $KE_z$ ; (b, d)  
 405 spectra of the divergent component  $KE_\Delta$ . In each case, the flow is further partitioned into low and high-frequency  
 406 motions as in Fig. 10. Panels (a) and (b) correspond to February, panels (c) and (d) to August.

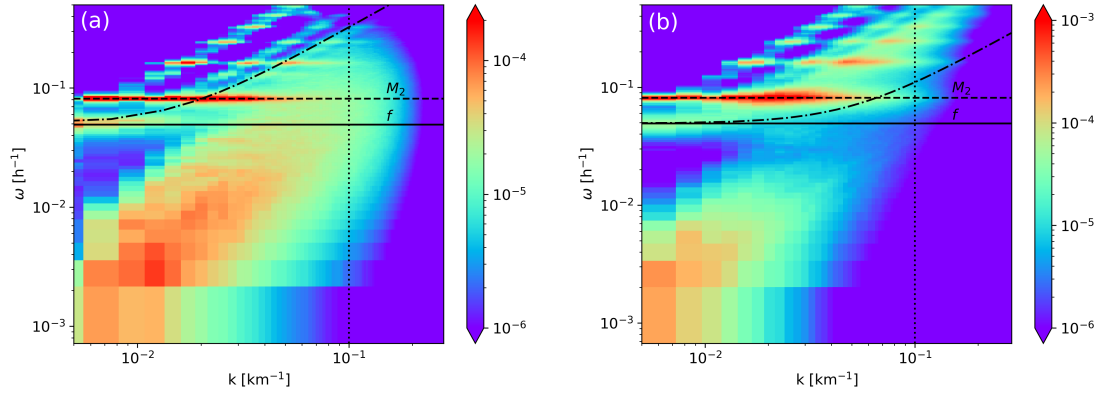
418 As in Kuroshio Extension, the wavenumber kinetic energy spectrum (Fig. 12a), is in both seasons  
 419 quite energetic at submesoscales. We note, however, that in this region the February and August  
 420 spectra are remarkably close (indeed, they are equal, within error bars) and scale approximately  
 421 as  $E(k) \sim k^{-2.4}$  over more than a decade. The summer spectrum is a bit more energetic and  
 422 steeper at large scales, while the winter one is slightly shallower, with a slope also compatible  
 423 with  $\beta = 2$  over a shorter wavenumber subrange. To quantify the scale-by-scale intensity of the  
 424 pair-dispersion process, we focus on the FSLE (Fig. 12b). The power-law and constant behaviors in  
 425 February and August, respectively, clearly indicate that dispersion is local in winter and nonlocal  
 426 in summer. Interestingly, from a quantitative point of view, we observe here the same season-  
 427 dependent agreement with the predictions from energy spectra as in Kuroshio Extension. Indeed,



412 FIG. 12. (a) Wavenumber spectra of horizontal kinetic energy in the Gulf Stream region, averaged over February  
 413 (blue squares) and August (red dots). For both months, the shaded areas represent the temporal variability of  
 414 the spectrum. (b) Corresponding FSLE  $\lambda(\delta)$  in the same region and for the same months. The  $\delta^{-0.3}$  scaling  
 415 law (short-dashed line) corresponds the spectrum  $E(k) \sim k^{-2.4}$ , while the  $\delta^{-2}$  scaling law (long-dashed line)  
 416 corresponds the diffusive limit. Uncertainties are estimated as the 95% confidence interval from a bootstrapping  
 417 procedure.

428 the winter scaling  $\lambda(\delta) \sim \delta^{-0.3}$  quite nicely matches the spectrum-based expectation  $\lambda(\delta) \sim \delta^{(\beta-3)/2}$   
 429 (with  $\beta = 2.4$ ), but the extended plateau,  $\lambda(\delta) \simeq \text{const}$ , found in summer is in evident contrast with  
 430 the corresponding spectrum, which would even indicate a different dispersion regime (local rather  
 431 than nonlocal).

432 As before, we then resort to frequency-wavenumber kinetic energy spectra to assess the relative  
 433 importance of high and low frequency motions in each season (Fig. 13). The global picture returned  
 434 by such spectra is very similar to the one found in Kuroshio Extension, which also confirms that  
 435 these two energetic regions share the same qualitative dynamical features. Specifically, M/SM  
 436 motions dominate the energetic content of the flow in February; in summer IGWs are considerably  
 437 more energetic than in winter, and in parallel the intensity of the flow at submesoscales gets  
 438 reduced. Minor quantitative differences among the two regions can also be noticed. For instance,  
 439 here the flow is less energetic, particularly in the submesoscale range in winter (as also observed  
 440 from the slightly steeper February wavenumber spectrum), with respect to that found in Kuroshio  
 441 Extension.

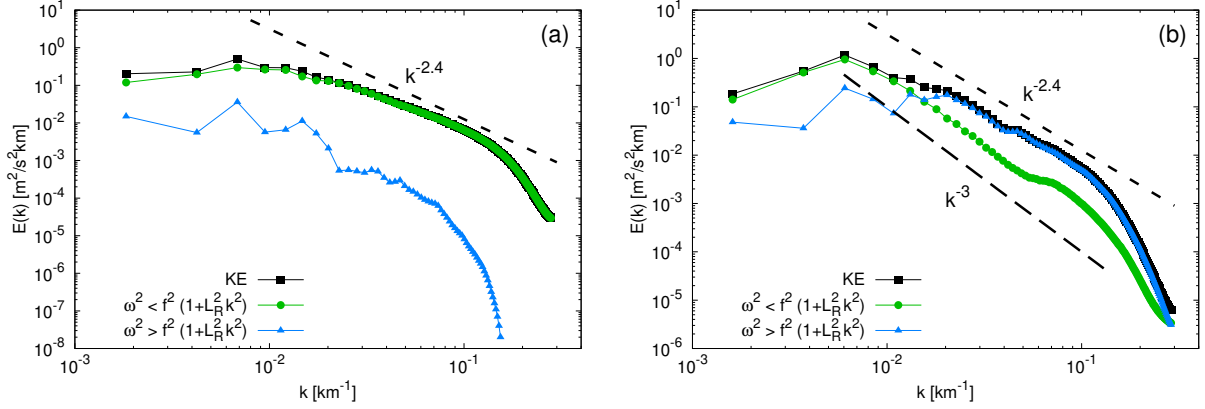


442 FIG. 13. Frequency-wavenumber spectra of kinetic energy  $E(k, \omega)$ , defined as in Fig. 9, in the Gulf Stream  
 443 region during February (a) and August (b). For the (dashed-dotted) curve representing the dispersion relation,  
 444 the deformation radii are  $L_R = 65$  km (a) and  $L_R = 20$  km (b).

448 Using the spatiotemporal spectra  $E(k, \omega)$ , we next compute the contributions of low and high-  
 449 frequency motions to the total wavenumber kinetic energy spectrum. The results, shown in Fig. 14  
 450 for both seasons, closely resemble those found in Kuroshio Extension. In winter, M/SM motions  
 451 [corresponding to frequencies  $\omega^2 < f^2(1 + L_R^2 k^2)$ ] essentially account for the full kinetic energy  
 452 at all scales and their spectrum is then close to  $k^{-2.4}$ . The summer spectrum is dominated by  
 453 the slow M/SM at scales larger than 50 – 100 km and by IGWs [corresponding to frequencies  
 454  $\omega^2 > f^2(1 + L_R^2 k^2)$ ] at smaller scales. The M/SM spectrum scales as  $k^{-3}$ , the IGW one as  $k^{-2.4}$ .  
 455 Therefore, the winter and summer energy spectra, when temporally filtered to retain only the  
 456 contribution from low-frequency motions, are respectively compatible with the observed local and  
 457 nonlocal dispersion regimes. This illustrates that the picture found in Kuroshio Extension might  
 458 be more general and, thus, confirms that while contributing to the kinetic energy spectrum, IGWs  
 459 are unlikely to have a measurable impact on relative dispersion, at least in the range of separations  
 460 explored in this study.

## 461 7. Conclusions

462 We investigated Lagrangian particle transport at the ocean surface, using the high-resolution  
 463 ocean general circulation model LLC4320, which incorporates internal tides in addition to meso  
 464 and submesoscale dynamics. We examined in details particle pair dispersion in the Kuroshio



445 FIG. 14. Decomposition of the wavenumber spectra of kinetic energy  $E(k)$  as in Fig. 10 for February (a) and  
 446 August (b) in the Gulf Stream region. The reference lines  $k^{-2.4}$  in (a),  $k^{-3}$  and  $k^{-2.4}$  in (b) are also shown for  
 447 comparison. The deformation radii are  $L_R = 65$  km (a) and  $L_R = 20$  km (b).

465 Extension in two different seasons. We then extended our analysis to another study region, close  
 466 to the Gulf Stream.

467 The surface velocities from the model were used to advect Lagrangian tracers over the months  
 468 of February and August (representative of winter and summer, respectively). The pair-dispersion  
 469 process was analyzed by means of two-particle statistical indicators, which allow to identify  
 470 different dispersion regimes and, in principle, to link the Lagrangian results and the Eulerian flow  
 471 properties via dimensional arguments developed in the framework of QG turbulence (LaCasce  
 472 2008; Foussard et al. 2017).

473 Our findings demonstrate that dispersion is local, meaning controlled by flow features having the  
 474 same size as the particle separation distance, in winter, and nonlocal, i.e. dominated by the largest  
 475 flow scales, in summer. This is most clearly revealed by the FSLE, measuring the scale-by-scale  
 476 dispersion rate, but it is also confirmed by other space or time-dependent diagnostics. In winter,  
 477 the observed behaviors of Lagrangian indicators, to fair extent, match the dimensional expectations  
 478 constructed from the slope of the wavenumber kinetic energy spectrum. In summer, however,  
 479 the predictions based on the spectrum are not confirmed by the actual Lagrangian statistics. The  
 480 disagreement is not only quantitative but also qualitative: based on the spectrum one would expect  
 481 local dispersion, while the analysis of particle trajectories indicates that dispersion is nonlocal.

482 Examination of spatiotemporal kinetic energy spectra revealed key to understand this apparent  
483 discrepancy in summer. Computing how energy is distributed among both wavenumbers and  
484 frequencies, indeed, allows to separate the contributions from the slower M/SM components of  
485 the flow and faster IGWs. Through this approach, we could show that the observed dispersion  
486 behaviors reasonably agree with the predictions based on the wavenumber kinetic energy spectrum  
487 associated with the slow, nearly balanced (and mainly rotational) part of the velocity field. In  
488 winter high-frequency motions marginally contribute to the spectrum. In summer, they dominate  
489 energetically only at scales smaller than roughly 50 km, and our results are consistent with the  
490 dispersion process being controlled by the more intense strain associated with the large-scale,  
491 lower-frequency flow and not by the high-frequency flow. No evidence of an impact of internal  
492 waves on pair dispersion was found in the LLC4320 simulation in the Kuroshio Extension region.  
493 This picture is further supported by the same analysis conducted in another energetic region, close  
494 to the Gulf Stream, sharing similar statistical properties of the Eulerian flow, where we essentially  
495 observed the same Lagrangian phenomenology.

496 Understanding how general these conclusions are remains an open point, and examining the  
497 geographic (and seasonal) variability of relative dispersion appears to us a valuable perspective  
498 for future work. To our knowledge, to date only few studies have addressed the impact of IGWs  
499 on Lagrangian tracer dispersion, and the conclusions appear varied. For instance, in a study using  
500 in-situ and synthetic surface drifters in the Gulf of Mexico (Beron-Vera and LaCasce 2016) it was  
501 argued that fixed lengthscale indicators, like the FSLE, should be affected by inertial oscillations,  
502 which, however, is not the case in our findings. It might then be interesting to correlate the  
503 Lagrangian dispersion properties observed in that region with the statistical features of the slow  
504 and fast components of the associated Eulerian flow. Another study by Tranchant et al. (2025)  
505 investigated drifter dispersion in an energetic meander of the Antarctic Circumpolar Current, over  
506 a specific period of time, where waves seem to be rather weak. By comparing with virtual drifters  
507 advected by SWOT velocities, the authors showed that balanced motions dominate dispersion at  
508 scales larger than  $\approx 10$  km. Those results, to some extent, align with ours in winter. It would seem  
509 to us interesting to complement them with an analysis over different periods and, again, perhaps  
510 an examination of spatiotemporal spectra from a high-resolution numerical model.

511 Simplified models and PE simulations in smaller domains may also reveal useful to gain further  
512 insight into the basic physical mechanisms and to estimate the critical lengthscale under which IGWs  
513 may become important for dispersion. Following this approach, Wang et al. (2018) investigated the  
514 destabilization of a circular front in the presence of a wealth on internal waves. While in that case  
515 the FSLE is sensitive to inertial oscillations, this effect is only observed at scales smaller than an  
516 inertial-oscillation scale  $V/f$ , where  $V$  is the typical velocity of Lagrangian particles. In our case,  
517 in August such lengthscale (4.59 km) is very close to the first separation value ( $\delta \approx 4.17$  km) used  
518 in the FSLE computation. A similarly crude estimate based on the semidiurnal tidal frequency,  
519  $M_2 > f$ , would give an even smaller typical length. Resolving smaller scales in the Lagrangian  
520 dispersion process would require quite a smaller initial pair separation (currently it is  $R_0 \approx 3.48$  km).  
521 For this, in turn, simulations at even higher spatial resolution than the present ones would be needed,  
522 considering that the inertial-oscillation scale is close to LLC4320 horizontal grid spacing, where  
523 numerical diffusivity smoothens the flow. These considerations explain, at least qualitatively, why  
524 our summer FSLE is insensitive to possible effects due to internal waves.

525 We conclude by shortly commenting on the implications of our results for the interpretation  
526 of the new, high-resolution altimetry data provided by SWOT. When high-frequency motions are  
527 relatively weak, as in our winter situations, the theoretical links between the spectral kinetic energy  
528 distribution of the Eulerian flow and relative-dispersion properties should reveal useful to predict  
529 the latter. Pending the geostrophic approximation is sufficiently accurate, the satellite-derived  
530 velocity field should enable more direct and local predictions of transport and dispersion via  
531 Lagrangian advection by the geostrophic velocity field. Note that Yu et al. (2021) and Demol  
532 et al. (2025) have quantified the validity of geostrophy at global scales from numerical models  
533 and observations, respectively. More studies are required in order to identify general conditions of  
534 validity, e.g. in terms of spatial/temporal scales and flow conditions, and hence verify our ability  
535 to estimate dispersion properties from SWOT and the nature of the signal processing required  
536 to do so. However, when internal waves are more important, as in summer in this study, it  
537 is unlikely that such theoretical links remain meaningful to obtain information about dispersion,  
538 unless high-frequency motions are filtered out from the satellite-derived velocities. Future missions  
539 such as Odyssea (Torres et al. 2023) may bring useful complementary information to estimate the  
540 low-frequency component of the flow required to assess ocean-surface Lagrangian dispersion.

541 *Acknowledgments.* This work was supported by the French Space Agency CNES (Centre National  
542 d'Etudes Spatiales) through the SWOT mission in the framework of DIEGO and DIEGOB projects.  
543 The dataset was analyzed on the Datarmor supercomputer at IFREMER in Brest.

544 *Data availability statement.* The data that support the findings of this study are available from  
545 the corresponding author upon reasonable request.

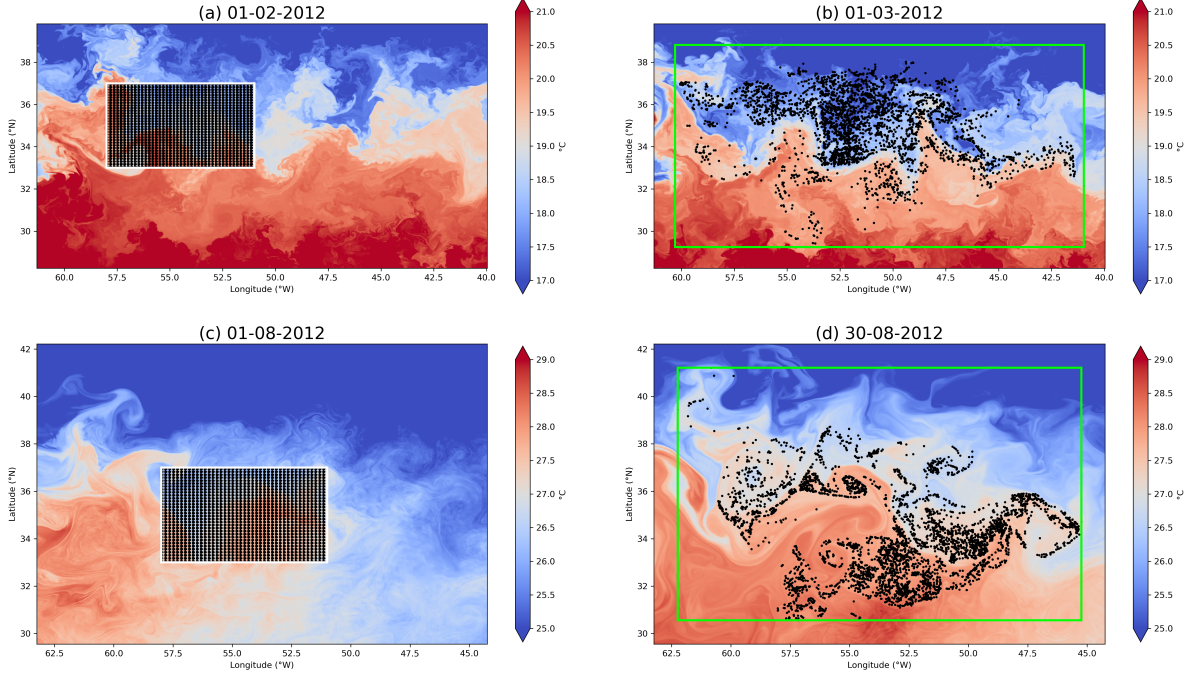
## 546 APPENDIX A

### 547 **Eulerian and Lagrangian analysis in the Gulf Stream region**

548 Here we present a more extensive characterization of the Eulerian flow properties and relative  
549 dispersion results in the Gulf Stream region, to contrast with those found in the Kuroshio Extension  
550 (see main text).

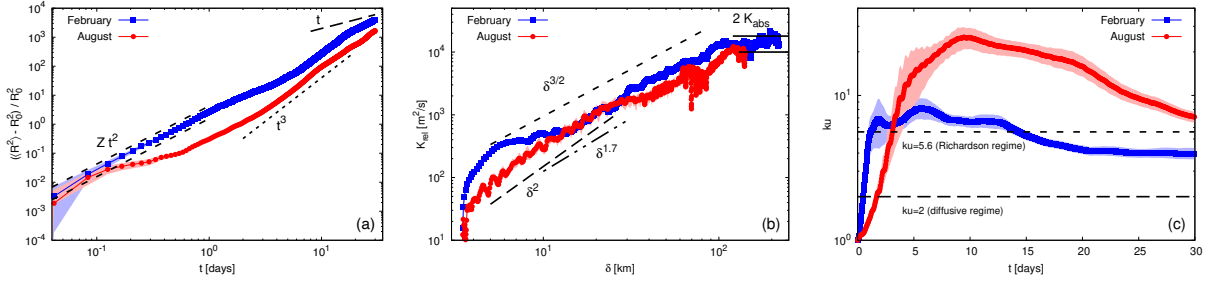
551 For both winter and summer, the particle distributions at the beginning and at the end of the  
552 1-month advection period, superimposed over the simultaneous SST fields, are shown in Fig. A1.  
553 In February (Fig. A1a), the flow is characterized by a lot of mixed-layer instabilities, which reveal  
554 themselves in the roll-up of SST fronts at the smallest scales. In August, the spatial organization of  
555 the temperature field is driven by the presence of mesoscale features, such as large-scale filaments  
556 (Fig. A1c). The overall picture is analogous to the one in Kuroshio Extension. Concerning  
557 the Lagrangian particle distribution, we see that, after one month, particles tend to spread more  
558 homogeneously in February, while they are more affected by the large-scale structures of the flow  
559 in summer (Figs. A1b, d). These patterns suggest that dispersion is more local (i.e. more affected  
560 by smaller-scale flow features) in winter than in summer.

568 Figure A2 shows complementary results from Lagrangian indicators completing those presented  
569 in Sec. 6, namely relative dispersion as a function of time, relative diffusivity versus the separation  
570 distance  $\delta = \langle R^2(t) \rangle^{1/2}$  and kurtosis versus time. The general trends are quite similar to those  
571 found in Kuroshio Extension. Relative dispersion at short times here shows a clearer agreement  
572 with the prediction  $Zt^2$  also in summer. In August, it later slows down [after  $t \approx (0.1 - 0.2)$  days],  
573 before approaching a growth close to  $t^3$  or slightly faster. In February,  $\langle R^2(t) \rangle$  is generally larger  
574 at intermediate times. Its subsequent behavior is not very far from that of August (roughly  $\sim t^3$ ),  
575 but less clear in terms of scaling. More generally, also in this region, it is not straightforward  
576 to identify dispersion regimes from this indicator. Relative diffusivity  $K_{rel}$ , when plotted against



561 FIG. A1. Snapshots of the SST field in the Gulf Stream region in February (top line) and in August (bottom line)  
 562 at the beginning (a, c) and at the end (b, d) of the 30-day Lagrangian advection experiments. The corresponding  
 563 particle distributions are shown with black dots. The green rectangles in (b, d) indicate the largest area covered  
 564 by particles on the latest day of the month.

577 the separation distance  $\delta = \langle R^2(t) \rangle^{1/2}$  more clearly allows to distinguish the winter and summer  
 578 dispersion regimes. In February,  $K_{rel}$  fluctuates around a  $\sim \delta^{3/2}$  law, between 10 and 100 km,  
 579 which would correspond to a spectrum  $E(k) \sim k^{-2}$ . Interestingly, however, in August we find a  
 580 rather clear  $\delta^2$  scaling from about 5 to 50 km, as one would expect for a spectrum steeper than  $k^{-3}$   
 581 and pointing to nonlocal dispersion. Beyond this range, diffusivity shows slower growth, possibly  
 582 suggestive of local dispersion, and roughly compatible with  $K_{rel} \sim \delta^{3/2}$  (or the close scaling  
 583  $K_{rel} \sim \delta^{1.7}$ , corresponding to  $\beta = 2.4$ , over a smaller subrange of separations). Correspondingly,  
 584 while in winter kurtosis quite soon attains a constant value close to 5.6 [the expectation for local,  
 585 Richardson dispersion, for which  $\langle R^2(t) \rangle \sim t^3$  and  $K_{rel}(\delta) \sim \delta^{4/3}$ ] and stays close to it for almost  
 586 all the advection period, in summer  $ku$  initially grows to a value 5 or 6 times larger, before starting  
 587 a low decay after about 10 days of advection. In the second half of August, these data do not allow



565 FIG. A2. Normalized relative dispersion vs time (a), relative diffusivity vs the separation distance  $\delta = \langle R^2(t) \rangle^{1/2}$   
 566 (b) and kurtosis vs time (c) in the Gulf Stream region, for February (blue squares) and August (red dots).  
 567 Uncertainties are estimated as the 95% confidence interval from a bootstrapping procedure.

568 to draw a safe conclusion on the dispersion regime, a longer simulation would be needed to clarify  
 569 this point.

## 590 References

- 591 Arbic, B. K., and Coauthors, 2022: Near-surface oceanic kinetic energy distributions from drifter  
 592 observations and numerical models. *J. Geophys. Res.*, **127**, e2022JC018551, [https://doi.org/](https://doi.org/0.1029/2022JC018551)  
 593 0.1029/2022JC018551.
- 594 Artale, V., G. Boffetta, A. Celani, M. Cencini, and A. Vulpiani, 1997: Dispersion of passive tracers  
 595 in closed basins: beyond the diffusion coefficient. *Phys. Fluids A*, **9**, 3162–3171, [https://doi.org/](https://doi.org/10.1063/1.869433)  
 596 10.1063/1.869433.
- 597 Aurell, E., G. Boffetta, A. Crisanti, G. Paladin, and A. Vulpiani, 1997: Predictability in the  
 598 large: an extension of the concept of Lyapunov exponent. *J. Phys. A*, **30**, 1–26, [https://doi.org/](https://doi.org/10.1088/0305-4470/30/1/003)  
 599 10.1088/0305-4470/30/1/003.
- 600 Babiano, A., C. Basdevant, P. L. Roy, and R. Sadourny, 1990: Relative dispersion  
 601 in two-dimensional turbulence. *J. Fluid Mech.*, **214**, 535–557, [https://doi.org/10.1017/](https://doi.org/10.1017/S0022112090000258)  
 602 S0022112090000258.
- 603 Barkan, R., K. B. Winters, and J. C. McWilliams, 2017: Stimulated imbalance and the enhance-  
 604 ment of eddy kinetic energy dissipation by internal waves. *J. Phys. Oceanogr.*, **47**, 181–198,  
 605 <https://doi.org/10.1175/JPO-D-16-0117.1>.

- 606 Batchelor, G. K., 1950: The application of the similarity theory of turbulence to atmospheric  
607 diffusion. *Q. J. R. Meteorol. Soc.*, **76**, 133–146, <https://doi.org/10.1002/qj.49707632804>.
- 608 Beron-Vera, F. J., and J. H. LaCasce, 2016: Statistics of simulated and observed pair separa-  
609 rations in the Gulf of Mexico. *J. Phys. Oceanogr.*, **46**, 2183–2199, [https://doi.org/10.1175/  
610 JPO-D-15-0127.1](https://doi.org/10.1175/JPO-D-15-0127.1).
- 611 Berti, S., F. A. Dos Santos, G. Lacorata, and A. Vulpiani, 2011: Lagrangian drifter dispersion  
612 in the southwestern Atlantic ocean. *J. Phys. Oceanogr.*, **41**, 1659–1672, [https://doi.org/10.1175/  
613 2011JPO4541.1](https://doi.org/10.1175/2011JPO4541.1).
- 614 Bühler, O., J. Callies, and R. Ferrari, 2014: Wave–vortex decomposition of one-dimensional  
615 ship-track data. *J. Fluid Mech.*, **756**, 1007–1026, <https://doi.org/10.1017/jfm.2014.488>.
- 616 Callies, J., R. Ferrari, J. M. Klymak, and J. Gula, 2015: Seasonality in submesoscale turbulence.  
617 *Nat. Commun.*, **6** (1), 6862, <https://doi.org/https://doi.org/10.1038/ncomms7862>.
- 618 Capet, X., P. Klein, B. L. Hua, G. Lapeyre, and J. C. McWilliams, 2008: Surface kinetic and  
619 potential energy transfer in SQG dynamics. *J. Fluid Mech.*, **604**, 165–174, [https://doi.org/  
620 10.1017/S0022112008001110](https://doi.org/10.1017/S0022112008001110).
- 621 Caspar-Cohen, Z., A. Ponte, N. Lahaye, E. D. Zaron, B. K. Arbic, X. Yu, S. LeGentil, and  
622 D. Menemenlis, 2025: Combining surface drifters and high resolution global simulations enables  
623 the mapping of internal tide surface energy. *Sci. Rep.*, **15** (1), 10672, [https://doi.org/https://  
624 //doi.org/10.1038/s41598-025-92662-w](https://doi.org/https://doi.org/10.1038/s41598-025-92662-w).
- 625 Cencini, M., and A. Vulpiani, 2013: Finite size Lyapunov exponent: review on applications. *J.*  
626 *Phys. A: Math. Theor.*, **46**, 254019, <https://doi.org/10.1088/1751-8113/46/25/254019>.
- 627 Corrado, R., G. Lacorata, L. Palatella, R. Santoleri, and E. Zambianchi, 2017: General character-  
628 istics of relative dispersion in the ocean. *Sci. Rep.*, **7**, 46291, <https://doi.org/10.1038/srep46291>.
- 629 Delandmeter, P., and E. Van Sebille, 2019: The Parcels v2.0 Lagrangian framework: new  
630 field interpolation schemes. *Geosci. Model Dev.*, **12** (8), 3571–3584, [https://doi.org/10.5194/  
631 gmd-12-3571-2019](https://doi.org/10.5194/gmd-12-3571-2019).

- 632 Demol, M., A. L. Ponte, P. Garreau, J.-F. Piollé, C. Ubelmann, and N. Rasclé, 2025: Diagnosis of  
633 ocean near-surface horizontal momentum balance from pre-SWOT altimetric data, drifter tra-  
634 jectories, and wind reanalysis. *Authorea Preprints*, [https://doi.org/10.22541/essoar.173687380.](https://doi.org/10.22541/essoar.173687380.01053119/v2)  
635 01053119/v2.
- 636 Döös, K., B. Jönsson, and J. Kjellsson, 2017: Evaluation of oceanic and atmospheric trajectory  
637 schemes in the TRACMASS trajectory model v6.0. *Geosci. Model Dev.*, **10** (4), 1733–1749,  
638 <https://doi.org/10.5194/gmd-10-1733-2017>.
- 639 Forget, G., J.-M. Campin, P. Heimbach, C. Hill, R. Ponte, and C. Wunsch, 2015: ECCO version  
640 4: An integrated framework for non-linear inverse modeling and global ocean state estimation.  
641 *Geosci. Model Dev.*, **8**, 3071–3104, <https://doi.org/10.5194/gmd-8-3071-2015>.
- 642 Foussard, A., S. Berti, X. Perrot, and G. Lapeyre, 2017: Relative dispersion in generalized two-  
643 dimensional turbulence. *J. Fluid Mech.*, **821**, 358–383, <https://doi.org/10.1017/jfm.2017.253>.
- 644 Fu, L.-L., and Coauthors, 2024: The surface water and ocean topography mission: a break-  
645 through in radar remote sensing of the ocean and land surface water. *Geophys. Res. Lett.*, **51**,  
646 e2023GL107652, <https://doi.org/10.1029/2023GL107652>.
- 647 Hakim, G. J., C. Snyder, and D. J. Muraki, 2002: A new surface model for cyclone–anticyclone  
648 asymmetry. *J. Atmos. Sci.*, **59**, 2405–2420, [https://doi.org/10.1175/1520-0469\(2002\)059%](https://doi.org/10.1175/1520-0469(2002)059%3C2405:ANSMFC%3E2.0.CO;2)  
649 [3C2405:ANSMFC%3E2.0.CO;2](https://doi.org/10.1175/1520-0469(2002)059%3C2405:ANSMFC%3E2.0.CO;2).
- 650 Hernández-Dueñas, G., M. Lelong, and L. M. Smith, 2021: Impact of wave–vortical interactions  
651 on oceanic submesoscale lateral dispersion. *J. Phys. Oceanogr.*, **51**, 3495–3511, [https://doi.org/](https://doi.org/10.1175/JPO-D-20-0299.1)  
652 <https://doi.org/10.1175/JPO-D-20-0299.1>.
- 653 Holmes-Cerfon, M., O. Bühler, and R. Ferrari, 2013: Particle dispersion by random waves in  
654 the rotating Boussinesq system. *J. Fluid Mech.*, **670**, 150–175, [https://doi.org/https://doi.org/10.](https://doi.org/10.1017/S0022112010005240)  
655 [1017/S0022112010005240](https://doi.org/10.1017/S0022112010005240).
- 656 Jones, C. S., Q. Xiao, R. P. Abernathey, and K. S. Smith, 2023: Using Lagrangian filtering to  
657 remove waves from the ocean surface velocity field. *J. Adv. Model. Earth Systems*, **15** (4),  
658 e2022MS003220, <https://doi.org/10.1029/2022MS003220>.

- 659 Klein, P., B. L. Hua, G. Lapeyre, X. Capet, S. LeGentil, and H. Sasaki, 2008: Upper ocean turbu-  
660 lence from high-resolution 3D simulations. *J. Phys. Oceanogr.*, **38**, 1748–1763, [https://doi.org/](https://doi.org/10.1175/2007JPO3773.1)  
661 10.1175/2007JPO3773.1.
- 662 LaCasce, J. H., 2008: Statistics from Lagrangian observations. *Prog. Oceanogr.*, **77**, 1–29,  
663 <https://doi.org/10.1016/j.pocean.2008.02.002>.
- 664 LaCasce, J. H., 2010: Relative displacement probability distribution functions from balloons and  
665 drifters. *J. Mar. Res.*, **68**, 433–457, <https://doi.org/10.1357/002224010794657155>.
- 666 Lange, M., and E. van Sebille, 2017: Parcels v0.9: prototyping a lagrangian ocean analysis  
667 framework for the petascale age. *Geosci. Model Dev.*, **10**, 4175–4186, [https://doi.org/10.5194/](https://doi.org/10.5194/gmd-10-4175-2017)  
668 [gmd-10-4175-2017](https://doi.org/10.5194/gmd-10-4175-2017).
- 669 Lapeyre, G., 2017: Surface quasi-geostrophy. *Fluids*, **2**, 7, <https://doi.org/10.3390/fluids2010007>.
- 670 Lumpkin, R., T. Özgökmen, and L. Centurioni, 2017: Advances in the applica-  
671 tion of surface drifters. *Ann. Rev. Marine Sci.*, **9**, 59–81, [https://doi.org/10.1146/](https://doi.org/10.1146/annurev-marine-010816-060641)  
672 [annurev-marine-010816-060641](https://doi.org/10.1146/annurev-marine-010816-060641).
- 673 Maalouly, M., G. Lapeyre, and S. Berti, 2024: Impact of ageostrophic dynamics on the pre-  
674 dictability of Lagrangian trajectories in surface-ocean turbulence. *Phys. Rev. Fluids*, **9**, 104 503,  
675 <https://doi.org/10.1103/PhysRevFluids.9.104503>.
- 676 Maalouly, M., G. Lapeyre, B. Cozian, G. Mompean, and S. Berti, 2023: Particle dispersion and  
677 clustering in surface ocean turbulence with ageostrophic dynamics. *Phys. Fluids*, **35**, 126 601,  
678 <https://doi.org/10.1063/5.0174665>.
- 679 Marshall, J., A. Adcroft, C. Hill, L. Perelman, and C. Heisey, 1997: A finite-volume, incompressible  
680 Navier Stokes model for studies of the ocean on parallel computers. *J. Geophys. Res.*, **102**, 5753–  
681 5766, <https://doi.org/10.1029/96JC02775>.
- 682 Morrow, R., L.-L. Fu, M.-H. Rio, R. R. Ray, P. Prandi, P.-Y. Le Traon, and J. Ben-  
683 veniste, 2023: Ocean circulation from space. *Surv. Geophys.*, **44**, 1243–1286, [https://doi.org/](https://doi.org/10.1007/s10712-023-09778-9)  
684 10.1007/s10712-023-09778-9.

- 685 Poje, A. C., and Coauthors, 2014: Submesoscale dispersion in the vicinity of the Deepwater  
686 Horizon Spill. *Proc. Natl. Acad. Sci. U. S. A.*, **111**, 12 693–12 698, [https://doi.org/10.1073/pnas.](https://doi.org/10.1073/pnas.1402452111)  
687 1402452111.
- 688 Rocha, C. B., T. K. Chereskin, S. T. Gille, and D. Menemenlis, 2016: Mesoscale to submesoscale  
689 wavenumber spectra in Drake passage. *J. Phys. Oceanog.*, **46**, 601–620, [https://doi.org/10.1175/](https://doi.org/10.1175/JPO-D-15-0087.1)  
690 JPO-D-15-0087.1.
- 691 Sasaki, H., P. Klein, B. Qiu, and Y. Sasai, 2014: Impact of oceanic-scale interactions on the seasonal  
692 modulation of ocean dynamics by the atmosphere. *Nat. Commun.*, **5** (1), 5636, [https://doi.org/](https://doi.org/https://doi.org/10.1038/ncomms6636)  
693 <https://doi.org/10.1038/ncomms6636>.
- 694 Sinha, A., D. Balwada, N. Tarshish, and R. Abernathey, 2019: Modulation of lateral transport  
695 by submesoscale flows and inertia-gravity waves. *J. Adv. Mod. Earth Syst.*, **11**, 1039–1065,  
696 <https://doi.org/10.1029/2018MS001508>.
- 697 Sutherland, B. R., 2010: *Internal Gravity Waves*. Cambridge University Press, [https://doi.org/](https://doi.org/10.1017/CBO9780511780318)  
698 [10.1017/CBO9780511780318](https://doi.org/10.1017/CBO9780511780318).
- 699 Torres, H., A. Wineteer, P. Klein, T. Lee, J. Wang, E. Rodriguez, D. Menemenlis, and H. Zhang,  
700 2023: Anticipated capabilities of the ODYSEA wind and current mission concept to estimate  
701 wind work at the air–sea interface. *Remote Sens.*, **15**, 3337, <https://doi.org/10.3390/rs15133337>.
- 702 Torres, H. S., P. Klein, D. Menemenlis, B. Qiu, Z. Su, J. Wang, S. Chen, and L.-L. Fu, 2018:  
703 Partitioning ocean motions into balanced motions and internal gravity waves: A modeling  
704 study in anticipation of future space missions. *J. Geophys. Res. Oceans*, **123**, 8084–8105,  
705 <https://doi.org/10.1029/2018JC014438>.
- 706 Torres, H. S., and Coauthors, 2022: Separating energetic internal gravity waves and small-  
707 scale frontal dynamics. *Geophys. Res. Lett.*, **49**, e2021GL096 249, [https://doi.org/10.1029/](https://doi.org/10.1029/2021GL096249)  
708 [2021GL096249](https://doi.org/10.1029/2021GL096249).
- 709 Tranchant, Y.-T., B. Legresy, A. Foppert, B. Pena-Molino, and H. E. Phillips, 2025: SWOT reveals  
710 fine-scale balanced motions and dispersion properties in the antarctic circumpolar current.  
711 *Authorea Preprints*, <https://doi.org/10.22541/essoar.173655552.25945463>.

- 712 Uchida, T., and Coauthors, 2024: Dynamic-mode decomposition of geostrophically balanced  
713 motions from swot altimetry. *ArXiv*, <https://doi.org/0.48550/arXiv.2407.09309>.
- 714 Wang, P., T. M. Özgökmen, and A. C. Haza, 2018: Material dispersion by oceanic internal waves.  
715 *Environ. Fluid Mech.*, **18**, 149–171, <https://doi.org/10.1007/s10652-016-9491-y>.
- 716 Yu, X., A. L. Ponte, S. Elipot, D. Menemenlis, E. D. Zaron, and R. Abernathey, 2019:  
717 Surface kinetic energy distributions in the global oceans from a high-resolution numerical  
718 model and surface drifter observations. *Geophys. Res. Lett.*, **46**, 9757–9766, [https://doi.org/](https://doi.org/10.1029/2019GL083074)  
719 [10.1029/2019GL083074](https://doi.org/10.1029/2019GL083074).
- 720 Yu, X., A. L. Ponte, N. Lahaye, Z. Caspar-Cohen, and D. Menemenlis, 2021: Geostrophy as-  
721 sessment and momentum balance of the global oceans in a tide-and eddy-resolving model. *J.*  
722 *Geophys. Res.*, **126**, e2021JC017422, <https://doi.org/10.1029/2021JC017422>.
- 723 Zhang, X., X. Yu, A. L. Ponte, Z. Caspar-Cohen, S. Le Gentil, L. Wang, and W. Gong, 2024:  
724 Lagrangian versus Eulerian spectral estimates of surface kinetic energy over the global ocean.  
725 *J. Geophys. Res.*, **129**, e2024JC021057, <https://doi.org/10.1029/2024JC021057>.